Very large remanent polarization in ferroelectric $Hf_{1-x}Zr_xO_2$ grown on Ge substrates by plasma assisted atomic oxygen deposition

C. Zacharaki[1,2], P. Tsipas[1], S. Chaitoglou[1], S. Fragkos[1], M. Axiotis[1], A. Lagoyiannis[1], R. Negrea[3], L. Pintilie[3], A. Dimoulas[1,*]

[1]*National Centre for Scientific Research "Demokritos", 15310, Athens, Greece*

[2]*Physics Department, National and Kapodistrian University of Athens, 15772, Athens, Greece*

[3]*National Institute for Materials Physics, 077125, Bucharest-Magurele, Romania*

Abstract

Plasma assisted atomic oxygen deposition was used to grow polycrystalline ferroelectric $Hf_{1-x}Zr_xO_2$ (x=0.5-0.7) on technologically important (100) Germanium (Ge) substrates showing sharp crystalline interfaces free of interfacial amorphous layers and strong evidence for the presence of a predominately orthorhombic phase. The electrical properties, evaluated using metal-ferroelectric-semiconductor capacitors (MFS) show symmetric and robust ferroelectric hysteresis with weak or no wake-up effects. The MFS with x=0.58 show very large remanent polarization up to 34.4 μC/cm^2, or 30.6 μC/cm^2 after correction for leakage and parasitics, combined with good endurance reaching 10^5 cycles at 2.3 MV/cm cycling field. The results show good prospects for the fabrication of Ge ferroelectric field effect transistors (FeFETs) for use in 1T FeFET embedded nonvolatile memory cells with improved endurance.

* *Corresponding author*: a.dimoulas@inn.demokritos.gr

Hafnium oxide is a key gate dielectric material for nanoelectronics since it enables the scaling of advanced complementary metal oxide semiconductor (CMOS) devices and circuits, enhancing their performance. The discovery of ferroelectricity in Hf and Zr-based oxides[1] opens new opportunities for Si-compatible embedded non-volatile ferroelectric memories[2-4] and creates the prospect for low power/high performance steep slope switches based on the concept of negative capacitance (NC)[5-7] in transistors with ferroelectric gates.

Metal-Ferroelectric-Metal (MFM) capacitors with ferroelectric (FE) $Hf_{1-x}Zr_xO_2$ (HZO) have received particular attention[8,9] mainly due to the compatibility of HZO (x~0.5) with low temperature processing requirements[10] of 1T-1C memory elements in the back-end of line (BEOL) of CMOS circuitry. On the other hand, ferroelectric field effect transistors (FeFETs) based on a metal-ferroelectric-semiconductor (MFS) structure offer unprecedented integration with CMOS in the front end of line (FEOL) and non-destructive reading in 1T-FeFET memory cells, suffering however from low endurance of about 10^4 cycles[2] when biased in the high retention regime, which is attributed to unwanted charge trapping at interfacial oxide layers. The research on HZO FeFETs[11] is currently accelerating[12-15] essentially driven by foreseen applications in the area of neuromorphic devices[16-18] and circuits either as emulators of biological neurons[18] or as electronic synapses[16,17] functioning as accelerators of deep neural network training[17].

Notably, neuromorphic devices have been demonstrated recently using Ge nanowire FeFET[19]with HZO ferroelectric, renewing interest in technologically important Ge channels/substrates with potential advantages for FeFET fabrication. Unlike HfO_2/Si where an unintentional (Hf)SiOx interfacial layer is spontaneously formed, Hf(Zr)O_2/Ge interfaces are typically clean[20,21] due to the fact that (Hf)GeOx

oxides are unstable, easily dissociating at moderate annealing temperatures thus leaving oxide-free crystalline interfaces. This could be beneficial for the improvement of endurance[2] and memory window[14] in FeFETs. In addition, Ge, as a low gap semiconductor has a large number of intrinsic free carriers which could screen the polarization charges thus stabilizing the FE domains in MFS structures. Unlike Si, work on Ge substrates[22-26] is rather limited to Ge FinFETs with HZO FE gates for NC FET[23], Y-doped HfO_2[24,25] and HZO on Ge for ferroelectric tunnel junctions (FTJ)[26]. Notably, in the latter work[26], 8 nm HZO MFS fabricated on Ge show the largest polarization of P_r ~ 18 μC/cm^2, compared to all others fabricated on TiN, Si, or SiGe substrates. It is anticipated that the low thermal expansion coefficient of Ge[26], and consequently the large thermal expansion coefficient mismatch with HZO produces an appreciable residual thermal tensile strain during cooling down from crystallization temperature to room temperature (RT). The latter tensile strain could stabilize the orthorhombic FE phase against the non-FE tetragonal or monoclinic phases as previously suggested[27,28] resulting in higher remanent polarization. For example, HZO sandwiched between thick TiN gate electrodes acting as tensile stressors[28] shows P_r ~ 26 μC/cm^2 which is the largest value obtained in MFM capacitors with atomic layer deposited (ALD) HZO[8,28,29]. There is increasing evidence that epitaxial strain influences ferroelectricity. For example, it has been recently reported[30] that HZO grown on crystalline LSMO templates adopts a rhombohedral phase as a result of epitaxial compressive strain which is ferroelectric yielding P_r~ 18 μC/cm^2 for a 9 nm thick HZO and a much higher P_r of 34 μC/cm^2 for a 5 nm-thick HZO. In addition, using microwave annealing of HZO/GeOx/Ge, the P_r is significantly enhanced suppressing also gate leakage in FETs and Ge interdiffusion[23]. Achieving large values of P_r in HZO-based devices is important since it gives more flexibility for the design and sensing of memory cells.

In this letter, we report on a very large P_r in TiN/$Hf_{1-x}Zr_xO_2$/Ge(x~0.58) MFS device layer structures where both the HZO and the TiN top metal gate are produced by plasma assisted atomic oxygen deposition (PA-AOD) in one growth run in a molecular beam epitaxy chamber.

HZO films were prepared by PA-AOD at 225°C on single crystal p-type (0.03 Ω·cm) Ge(100) substrates. Prior to deposition, Ge substrates were annealed at 500°C for 30 mins in vacuum to obtain a clean surface free of C and O contaminants. The HZO films were deposited by co-evaporating Hf and Zr metals from two different electron guns in the presence of reactive atomic oxygen generated by a remote *rf* plasma source at 350 Watt and O_2 partial pressure of 6×10^{-6} Torr. In-situ RHEED indicates polycrystalline material. Nominally 10-nm-thick TiN metal were grown on top of HZO films without breaking vacuum at room temperature, 270°C, 385°C with an evaporation Ti rate of 0.2 Å/sec and *rf* plasma at 350 Watt. To fabricate the MFS capacitors, Ti(5nm)/Pt(40nm) metal contacts were deposited on the Ge/HZO/TiN device layer structures either by shadow masking or by photolithography producing 300 μm and 50 μm dots, respectively. Subsequently, the samples received rapid thermal annealing (RTA) at 750°C for 20 sec in N_2 and a ramp-up rate of 150°C/sec. Finally the TiN layer is selectively etched by $NH_4OH/H_2O_2/H_2O$ or H_2SO_4/H_2O_2 solution to finalize the Ge MFS capacitor.

The structure parameters and measured performance characteristics of the various MFS capacitors are summarized in Table I. In order to extract the Zr composition x in HZO films, Rutherford Backscattering Spectroscopy (RBS) measurements were conducted at the microprobe setup installed at the 5.5 MV Tandem accelerator of the Institute of Nuclear and Particle Physics, NCSR "Demokritos". The samples were irradiated with a 1.4 MeV deuteron which was focused to a beam spot of

50×50 μm^2 on target. The backscattered deuterons were detected with the aid of a SSB detector placed at 150° with respect to the beam axis. The acquired spectra (Fig.1) were analyzed using the SIMNRA code[31].

The MFS structures with x=0.58 were characterized by High Resolution Transmission Electron Microscopy (HRTEM) and Selected Area Electron Diffraction (SAED) (Fig.2) on specimens prepared by focused ion beam (FIB). The HZO and TiN layers are uniform and continuous each with thickness of ~13 nm and have roughness less than 1 nm and 3 nm respectively (Fig. 2a). The HZO layers are polycrystalline (Fig. 2b,c) with a domain size in the range between 20 and 30 nm. Sharp crystalline interfaces are observed (Fig. 2c), free of interfacial amorphous oxide layers, in distinct contrast with the HZO/Si interfaces[15] where an amorphous interfacial oxide >1 nm is typically formed. The SAED diffraction pattern (Fig. 2b) reveals the presence of orthorhombic phase ((111)o diffraction spots), while diffraction from monoclinic phase could not be detected. This indicates that the HZO film is predominately orthorhombic.

Based on previous works on the role of tensile strain[27,28], it is anticipated that a predominately orthorhombic phase here in this work is stabilized by residual thermal tensile strain $\varepsilon \approx +\delta\gamma \cdot \delta T \approx 0.3\%$ due to a sizeable thermal expansion coefficient mismatch $\delta\gamma \equiv \gamma_{HZO}-\gamma_{Ge} = 4.1\cdot 10^{-6}$ K^{-1} ($\gamma_{HZO} \sim 1\cdot 10^{-5}$K^{-1} [32] and $\gamma_{Ge} = 5.9\cdot 10^{-6}$ K^{-1} [27]) and a temperature difference δT=725K between the crystallization annealing temperature T_{ann}=1023K and room temperature. It should be noted that the clean, crystalline interfaces (Fig. 2c) may promote the build-up of the thermal tensile strain as the HZO contracts faster than Ge during cooling down.

Dynamic P-E measurements at 1kHz were performed using an aixAcct Systems TF Analyzer 1000 and the main hysteresis characteristics are shown in Fig. 3. The Ge MFS hysteresis in the present work is more symmetric compared to Si MFS[15]. All

hysteresis curves show weak or no "wake-up" effects. In the MFS of Fig, 3, the coercive field E_c is 1.8MV/cm. With an exception of the 9-nm-thick film where the E_c is abnormally high (3.4MV/cm, Table I) more generally in our PA-AOD films E_c varies in the range between 1.3 and 2.0 MV/cm which is notably larger than the E_c values(~1MV/cm)[8] reported for HZO MFM capacitors grown by ALD. We anticipate that the large value of E_c in our MFS is indicative of reduced (interfacial) defects typically obtained in high quality epitaxial[30] thin films. The high E_c of 1.8MV/cm may be beneficial for FeFETs increasing the memory window (MW)[2] to about 4.7V, according to $MW=2d_{HZO}E_c$.

The largest value of remanent polarization P_r=34.4μC/cm^2 for E_{max}=3.8MV/cm (V_{max} =5 V) is obtained (Fig. 3) in the13-nm-thick sample with x=0.58. Other devices with higher (x=0.66, 0.7) and lower (x=0.5) Zr compositions also give robust and symmetric hysteresis, although with reduced but appreciable remanent polarization, typically larger than 20μC/cm^2 (see Table I). The large P_r is attributed to the predominant FE orthorhombic phase as detected by TEM/SAED (Fig. 2b)

Despite the large P_r in Fig.3 of the x=0.58 MFS capacitors the I-E measurements show that there is appreciable leakage, which may affect the P_r yielding erroneous results. To correct for leakage and possible contribution from parasitic charges, positive up-negative down (PUND) method[33] was used comprising a "write" pulse and a sequence of positive and negative "read" pulses as shown in Fig. 4a. Fig. 4b,c show the main characteristics of one of the MFS capacitors with x=0.58. It can be seen that the non-ferroelectric contribution (green and light blue excursions) is a small portion of the total polarization and displacement current, yielding, after correction (black curves), a nearly ideal hysteresis (Fig. 4b) and current (Fig. 4c) with a small (12.1 %) reduction in the remanent polarization from a value of P_r = 34.8 μC/cm^2 to a value of $P_{r,\,corr}$= 30.6

μC/cm^2 after correction. This indicates that most of the measured polarization is due to the ferroelectric switching with only minor contribution from parasitic charges and leakage. The value of 30.6 μC/cm^2 is among the largest P_r reported for HZO. More specifically the attained P_r in the present work is larger than those obtained in ALD HZO MFM[8,28] which are typically around 20 μC/cm[28], only exceptionally reaching 26 μC/cm^2 [28]. Our P_r values are also larger than those measured in HZO Ge FTJ [26] devices. Ultrathin (5 nm) epitaxial HZO on LSMO substrates[30] show larger (corrected) P_r~ 34 μC/cm^2, but thicker (9 nm) HZO layers on LSMO[30] show much reduced values of P_r ~ 18 μC/cm^2, which are lower than the ones observed in the present work.

In order to investigate the reliability and endurance of the ferroelectric devices, field cycling tests were carried out. The results for the13-nm-thick sample with x=0.58 composition at two different cycling field amplitudes are shown in Fig.5. Although the wake-up effects are relatively weak, fatigue appears after 1000 cycles for cycling field of 2.3 MV/cm before the devices breakdown after 100 000 cycles. Note however that despite fatigue, the P_r value remains well above 10 μC/cm^2 maintaining an acceptable window until it reaches breakdown. For larger fields (3.1 MV/cm), the devices break down after ~1000 cycles. After this point and at negative bias corresponding to a forward-biased p-type MFS diode, the leakage current increases and the hysteresis is distorted (Fig. 5c) developing a pronounced bump. The *dc* leakage, confirmed by I-E measurements, is considered to be the primary reason for the breakdown of MFS capacitors since HZO becomes essentially a resistor after further cycling beyond 1000.

MFM devices with ALD HZO generally show endurance larger than 10^9 cycles[9,14], however in MFS capacitors the situation is different. In the latter devices, the presence of a semiconductor (S) at the bottom electrode has adverse impact on endurance. Therefore FeFETs which are based on MFS structure show much lower

endurance[2], typically in the order of 10^4 -10^5. Our endurance results (10^5 cycles at 2.3 MV/cm) compare favorably with the endurance in FeFETs. Our results also compare favorably with cycling behavior of 8nm HZO FTJs with Ge bottom electrode[26] although charge transport and associated breakdown mechanisms in thin FTJs are different compared to the thicker HZO (>10 nm) Ge MFS diodes studied in the present work, so a direct and fair comparison is not feasible.

In summary, our Ge MFS capacitors with HZO and TiN top electrode, both grown by plasma assisted atomic oxygen deposition in one growth step, show excellent hysteresis characteristics with relatively high coercive field, little or no wake-up effects and with only small contribution from parasitic polarization effects, exhibiting a very large remanent polarization and good endurance when compared with the endurance of other MFS or FeFETs. It is anticipated that the high remanent polarization is due to predominance of the orthorhombic phase verified by TEM/SAED, which is likely stabilized as a result of residual thermal tensile strain originating from the Ge substrate. These performance and reliability characteristics in combination with the sharp crystalline HZO/Ge interfaces probed by TEM create the prospect that Ge FeFETs can be fabricated that overcome the short-comings of Si-based FeFETs which show limited endurance and reduced experimental memory window.

Acknowledgements: The authors acknowledge financial support from the European Union Horizon 2020, contract No 780302 -3eFERRO. The authors thank Dr. Ionel Mercioniu and Dr. Aurel Mihai Vlaicu from NIMP who prepared the TEM specimens by FIB; they also thank Dr. Uwe Schroeder of NaMLab and Dr. Igor Stolichnov of EPFL for very useful discussions.

REFERENCES

1) T. S. Böscke, J. Müller, D. Bräuhaus, U. Schröder, and U. Böttger, *Appl. Phys. Lett.* **99**, 102903 (2011)

2) J. Müller, P. Polakowski, S. Mueller, and T. Mikolajick, *ECS J. Sol. St. Sci. Technol*. **4**, N30 (2015)

3) M. H. Park, Y. H. Lee, H. J. Kim, Y. J. Kim, T. Moon, K. D. Kim, J. Müller, A. Kersch, U. Schroeder, T. Mikolajick, and C. S. Hwang, *Adv. Mat*. **27**, 1811 (2015)

4) L. Chen, T. Wang, Y. Dai, M. Cha, H. Zhu, Q. Sun, S. Ding, P. Zhou, L. Chua, and D. W. Zhang, *Nanoscale* **10**, 15826(2018)

5) S. Salahuddin, and S. Datta, *NanoLett*. **8** , 405 (2008)

6) M. M. Hoffmann, M. Pešić, K. Chatterjee, A. I. Khan, S. Salahuddin, S. Slesazeck, U. Schroeder, and T. Mikolajick, *Adv. Funct. Mater*. **26**, 8643 (2016)

7) M. Kombayashi, *Appl. Phys. Express* **11**, 110101 (2018)

8) S. J. Kim, J. Mohan, S. R. Summerfelt, and J. Kim, *JOM* **71**, 246 (2018)

9) M. H. Park, Y. H. Lee, T. Mikolajick, U. Schroeder, and C. S. Hwang, *MRS Communications* **8**, 795 (2018)

10) E. O'Connor, M. Halter, F. Eltes, M. Sousa, A. Kellock, S. Abel, and J. Fompeyrine, *APL Mater*. **6**, 121103 (2018)

11) S. Mueller, S. R. Summerfelt, J. Muller, U. Schroeder, and T. Mikolajick, *IEEE EDL* **33**, 185 (2012)

12) M. Trentzsch, S. Flachowsky, R. Richter, J. Paul, B. Reimer, D. Utess, S. Jansen, H. Mulaosmanovic, S. Müller, S. Slesazeck, J. Ocker, M. Noack, J. Müller, P. Polakowski, J. Schreiter, S. Beyer, T. Mikolajick, and B. Rice, *IEDM* 2016, p. 294

13) S. Dünkel, M. Trentzsch, R. Richter, P. Moll, C. Fuchs, O. Gehring, M. Majer, S. Wittek, B. Müller, T. Melde, H. Mulaosmanovic, S. Slesazeck, S. Müller, J. Ocker, M. Noack, D.-A. Löhr, P. Polakowski, J. Müller, T. Mikolajick, J. Höntschel, B. Rice, J. Pellerin, and S. Beyer, *IEDM 2017*, p. 485

14) K. Ni, P. Sharma, J. Zhang, M. Jerry, J. A. Smith, K, Tapily, R. Clark, S. Mahapatra, and S. Datta, *IEEE TED* **65**, 2461 (2018)

15) B. Zeng, W. Xiao, J. Liao, H. Liu, M. Liao, Q. Peng, S. Zheng, and Y. Zhou, *IEEE EDL* **39**, 1508 (2018)

16) H. Mulaosmanovic, J. Ocker, S. Müller, M. Noack, J. Müller, P. Polakowski, T. Mikolajick, and S. Slesazeck, *VLSI 2017,* p. T176

17) M. Jerry, P.-Y. Chen, J. Zhang, P. Sharma, K. Ni, S. Yu, and S. Datta, *IEDM 2017*, p. 139

18) H. Mulaosmanovic, E. Chicca, M. Bertele, T. Mikolajick, and S. Slesazeck, *Nanoscale* **10**, 21755 (2018)

19) W. Chung, M. Si, and P. D. Ye, *IEDM* 2018, p. 344

20) A. Dimoulas, G. Mavrou, G. Vellianitis, E. Evangelou, and N. Boukos, *Appl. Phys. Lett.* **86**, 032908 (2005)

21) A. Dimoulas, D. P. Brunco, S. Ferrari, J. W.Seo, Y. Panayiotatos, A. Sotiropoulos, T. Conard, M. Caymax, S. Spiga, M. Fanciulli, Ch. Dieker, E. K. Evangelou, S. Galata, M. Houssa, and M. M. Heyns, *Thin Sol. Films* **515**, 6337 (2007)

22) P. D. Lomenzo, Q. Takmeel, C. M. Fancher, C. Zhou, N. G. Rudawski, S. Moghaddam, J. L. Jones, and T. Nishida, *IEEE Electron Device Lett.* **36**, 766 (2015)

23) C. -J. Su, Y. -T Tang, Y.-C. Tsou, P.-J. Sung, F.-J. Hou, C.-J. Wang, S.-T. Chung, C.-Y. Hsieh, Y.-S. Yeh, F.-K. Hsueh, K.-H. Kao, S.-S. Chuang, C.-T. Wu, T.-Y. You, Y.-L. Jian, T.-H. Chou, Y.-L. Shen, B.-Y. Chen, G.-L. Luo, T.-C. Hong, K.-P. Huang, M.-C. Chen, Y.-J. Lee, T.-S. Chao, T.-Y. Tseng, W.-F. Wu, G.-W. Huang, J.-M. Shieh, W.-K. Yeh, and Y.-H. Wang, *VLSI* 2017, p. T152

24) X. Tian, L. Xu, S. Shibayama, T. Nishimura, T. Yajima, S. Migita, and A. Toriumi, *IEDM* 2017, 816

25) X. Tian, S. Shibayama, T. Nishimura, T. Yajima, S. Migita, and A. Toriumi, *Appl. Phys. Lett*. **112**, 102902 (2018)

26) Y. Goh, and S. Jeon, *Nanotechnology* **29**, 335201 (2018)

27) M. H. Park, H. J. Kim, Y. J. Kim, T. Moon, and C. S. Hwang, *Appl. Phys. Lett*. **104**, 072901 (2014)

28) S. J. Kim, D. Narayan, J.-G. Lee, J. Mohan, J. S. Lee, J. Lee, H. S. Kim, Y.-C. Byun, A. T. Lucero, C. D. Young, S. R. Summerfelt, T. San, L. Colombo, and J. Kim, *Appl. Phys. Lett*. **111**, 242901 (2017)

29) S. J. Kim, J. Mohan, J. Lee, J. S. Lee, A. T. Lucero, C. D. Young, L. Colombo, S. R. Summerfelt, T. San, and J. Kim, *Appl. Phys. Lett*. **112**, 172902 (2018)

30) Y. Wei, P. Nukala, M. Salverda, S. Matzen, H. J. Zhao, J. Momand, A. S. Everhardt, G. Agnus, G. R. Blake, P.Lecoeur, B. J. Kooi, J. Íñiguez, B. Dkhil, and B. Noheda, *Nat. Mater*. **17**, 1095 (2018)

31) M. Mayer, AIP Conf. Proc. **475**, 541(1999)

32) R. P. Haggerty, P. Sarin, Z. D. Apostolov, P. E. Driemeyer, and W. M. Kriven, *J. Am. Ceram. Soc*. **97**, 2213 (2014)

33) S. Bernacki, L. Jack, Y. Kisler, S. Collins, S. D. Bernstein, R. Hallock, B. Armstrong, J. Shaw, J. Evans, B. Tuttle, B. Hammetter, S. Rogers, B. Nasby, J. Henderson, J. Benedetto, R. Moore, Cpt R. Pugh, and A. Fennelly, *Integrated Ferroelectrics* **3**,97 (1993)

CAPTIONS:

Table I: In all samples HZO layers are grown at T_g=225 °C and received crystallization RTA at 750 °C for 20 sec with a ramp up rate of 150 °C/sec. The Zr composition x is determined by RBS. Thickness is nominal estimated from deposition rates which have been calibrated by XRR measurements, except for x=0.58 HZO whose thickness is measured by TEM. For remanent polarization, values corrected for leakage and parasitics by PUND measurements are given in parentheses.

Figure 1: RBS measurements for one of the samples using 1.4 MeV deuteron primary beams. By fitting the experimental data the Zr composition x=0.5 is determined.

Figure 2: (a) Cross section TEM image of MFS with Zr composition x=0.58 on a specimen prepared by FIB, (b) SAED pattern corresponding to TEM in (a). Arrows show the orthorhombic (111) diffraction spots. (c) HRTEM image of Ge/HZO/TiN/Ti-Pt heterostructure.

Figure 3: (a) Polarization (P) and (b) displacement current (I) vs electric field measurements (1kHz) for 2.3, 3.1 and 3.8 MV/cm field amplitude for a pristine 13-nm-thick HZO with composition x= 0.58.

Figure 4: (a) Sequence and shape of applied electrical pulses in PUND measurement. Polarization P (b), displacement current I (c) versus electric field E curves for a pristine 16-nm-thick HZO with composition x= 0.58 at E_{max}=2.8 MV/cm. Red curve corresponds to a first positive switching read pulse, magenta and blue to switching read pulses, green and light blue to non-switching read pulses and black are corrected ferroelectric hysteresis curves obtained by subtraction of parasitic contributions (non-switching pulses) from total polarization (switching pulses).

Figure 5: (a) Field cycling measurement for a 13-nm-thick sample with composition x= 0.58. Impact of field cycling on hysteresis loop at (b) 2.3 and (c) 3.1 MV/cm.

TABLES

Zr composition x	Thickness (nm)	TiN growth T (°C)	Remanent polarization P_r ($\mu C/cm^2$)	Coercive field E_c (MV/cm)
0.66	16	270	21.1(17.9)	1.5
0.58	13	RT	34.4(30.6)	1.8
0.50	16	385	21.7	1.9
0.70	9	RT	18.6	3.4

TABLEI

FIGURES

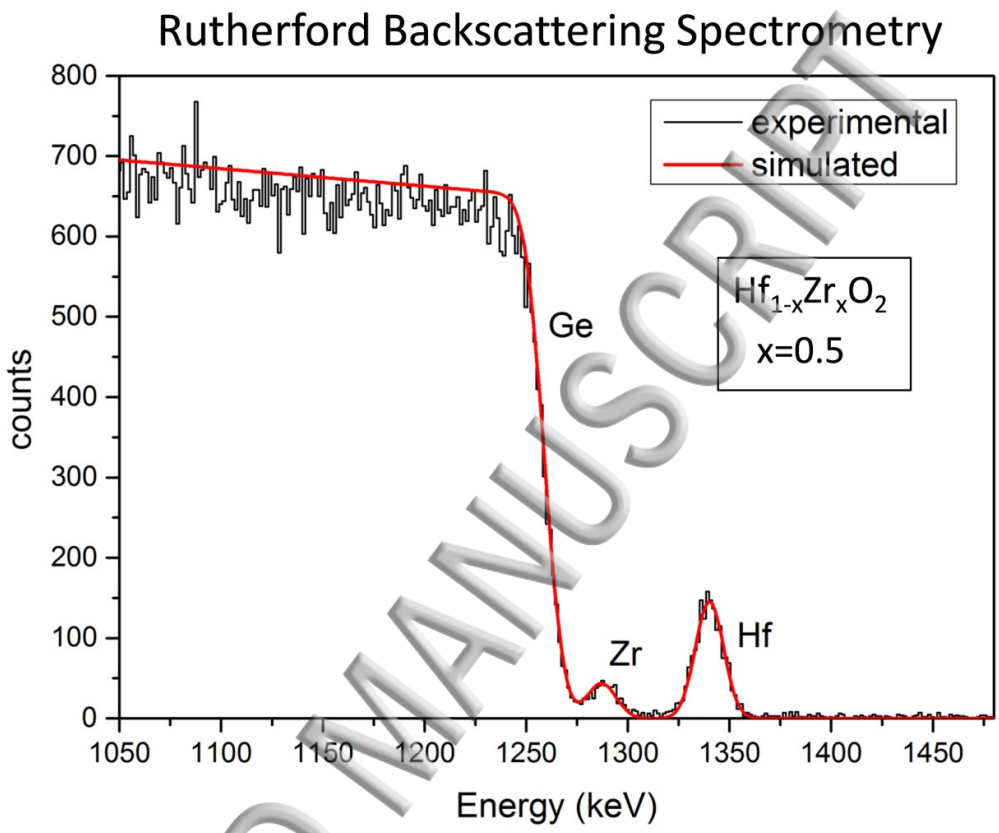

FIGURE 1

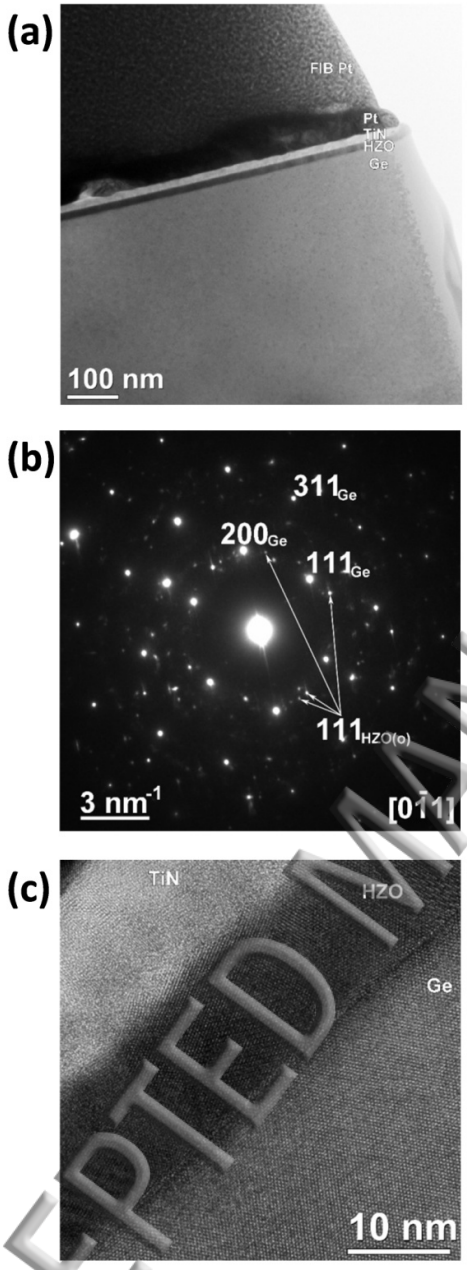

FIGURE 2

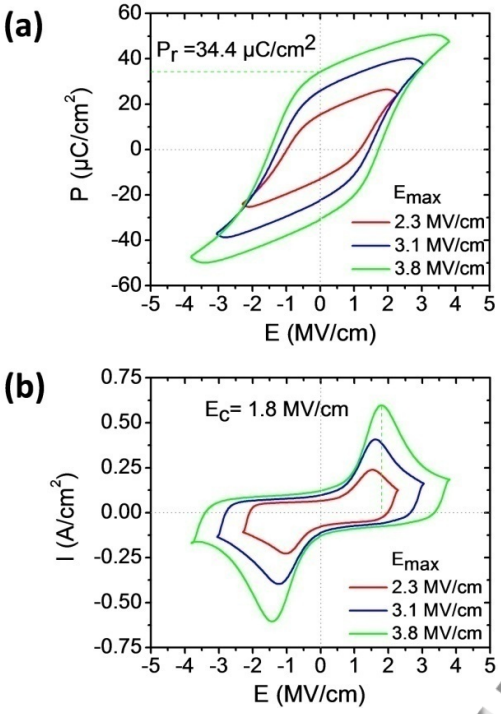

FIGURE 3

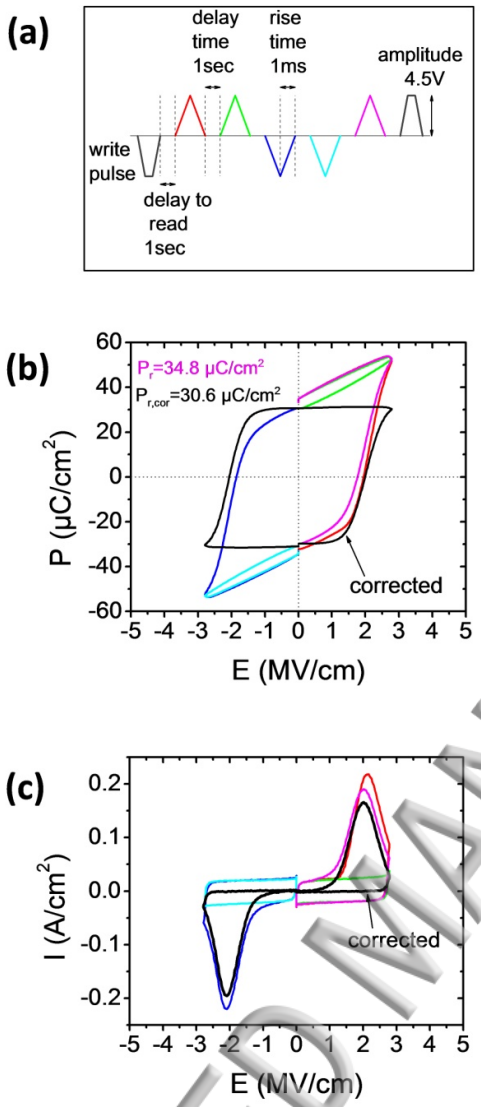

FIGURE 4

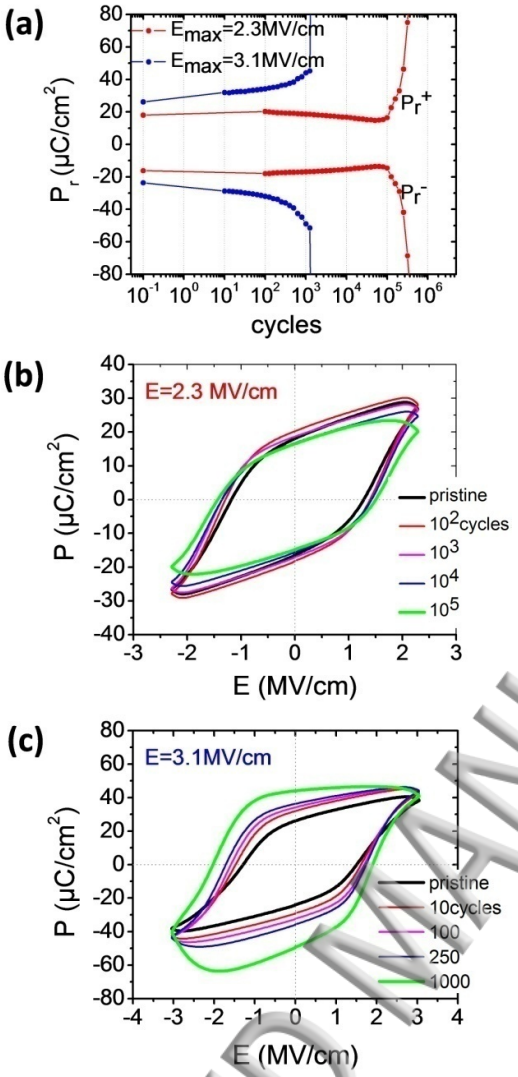

FIGURE 5

Rutherford Backscattering Spectrometry